PNAS RESEARCH ARTICLE | ENGINEERING

Mechanical cloak via data-driven aperiodic metamaterial design

Liwei Wang[a,b], Jagannadh Boddapati[c], Ke Liu[c,d], Ping Zhu[a,1], Chiara Daraio[c,1], and Wei Chen[b,1]

Edited by David Weitz, Harvard University, Cambridge, MA; received December 8, 2021; accepted February 13, 2022

Mechanical cloaks are materials engineered to manipulate the elastic response around objects to make them indistinguishable from their homogeneous surroundings. Typically, methods based on material-parameter transformations are used to design optical, thermal, and electric cloaks. However, they are not applicable in designing mechanical cloaks, since continuum-mechanics equations are not form invariant under general coordinate transformations. As a result, existing design methods for mechanical cloaks have so far been limited to a narrow selection of voids with simple shapes. To address this challenge, we present a systematic, data-driven design approach to create mechanical cloaks composed of aperiodic metamaterials using a large precomputed unit cell database. Our method is flexible to allow the design of cloaks with various boundary conditions, multiple loadings, different shapes and numbers of voids, and different homogeneous surroundings. It enables a concurrent optimization of both topology and properties distribution of the cloak. Compared to conventional fixed-shape solutions, this results in an overall better cloaking performance and offers unparalleled versatility. Experimental measurements on additively manufactured structures further confirm the validity of the proposed approach. Our research illustrates the benefits of data-driven approaches in quickly responding to new design scenarios and resolving the computational challenge associated with multiscale designs of functional structures. It could be generalized to accommodate other applications that require heterogeneous property distribution, such as soft robots and implants design.

mechanical cloaking | metamaterials | data-driven design | multiscale optimization

Significance

An invisibility cloak to conceal objects from an outside observer has long been a subject of interest in metamaterial design. While cloaks have been manufactured for optical, thermal, and electric fields, limited progress has been made for mechanical cloaks. Most existing designs rely on mapping-based methods, which have so far been limited to special base cells and a narrow selection of voids with simple shapes. In this study, we develop a fundamentally different approach by exploiting data-driven designs to offer timely, customized solutions to mechanical cloaking that were previously difficult to obtain. Through simulations and experimental validations, we show that excellent cloaking performance can be achieved for various boundary conditions, shapes of voids, base cells, and even multiple voids.

Metamaterials derive their properties mainly from the geometrical design of their microstructure besides their constituent materials (1–6). Metamaterials have been suggested for different functionalities in a wide range of applications, such as light-weight frames, biomimetic soft actuators, solar tracking systems, superlenses, and invisibility cloaks (7–14). As a representative application, cloaking materials could be used to conceal objects within a homogeneous surrounding, to prevent the detection of the objects with external physical fields, such as electromagnetic and mechanical fields (7, 13–15). To achieve a cloaking effect, a cloak is designed around the object or void, with its material properties different from those of the surrounding homogeneous material (Fig. 1*A*). A common approach for designing cloaks is through material-parameter transformation, by exploiting the form invariance of governing equations under transformation to decide material properties within the cloak region (8, 16–18). This approach has been successfully applied to, for example, cloaks for electromagnetic/optical waves (19), static electricity (20), and heat conduction (21, 22). However, material-parameter transformation is not applicable to mechanical cloaks that conceal elastic responses, e.g., displacement field and elastic waves. This is because the theory of continuum mechanics is not form invariant under general coordinate transformations—a prerequisite to use the material-parameter transformation (23). Moreover, to characterize the mechanical response of materials, a four-rank elasticity tensor is required, which adds complications to the cloaking design problem, compared to designing the scalar material parameters in other physical problems. Mathematical derivation suggests that a perfect mechanical cloak requires microstructures to achieve special anisotropic Cosserat tensor distributions, which might not be physically achievable (23, 24). As a result, limited progress has been made in designing mechanical cloaks (24–27).

Although a theoretically perfect mechanical cloaking could not be achieved in reality, one can still obtain an approximate mechanical cloaking under some necessary assumptions and constraints, within a narrow tolerance. Along this line, to bypass the requirement of form-invariant equations in designing mechanical cloaks, a direct lattice point-transformation approach was developed for a special bimode lattice metamaterial (24, 26, 28). Relying on a qualitative analog between electric conduction and mechanics, this approach heuristically applies spatial coordinate transformation on the lattice points,

Author affiliations: [a]The State Key Laboratory of Mechanical System and Vibration, School of Mechanical Engineering, Shanghai Jiao Tong University, Shanghai 200240, China; [b]Department of Mechanical Engineering, Northwestern University, Evanston, IL 60208; [c]Division of Engineering and Applied Science, California Institute of Technology, Pasadena, CA 91105; and [d]Department of Advanced Manufacturing and Robotics, Peking University, Beijing 100871, China

Author contributions: L.W., J.B., K.L., P.Z., C.D., and W.C. designed research; L.W., J.B., and K.L. performed research; L.W., J.B., K.L., P.Z., C.D., and W.C. analyzed data; and L.W., J.B., K.L., P.Z., C.D., and W.C. wrote the paper.

The authors declare no competing interest.

This article is a PNAS Direct Submission.

Copyright © 2022 the Author(s). Published by PNAS. This article is distributed under Creative Commons Attribution-NonCommercial-NoDerivatives License 4.0 (CC BY-NC-ND).

[1]To whom correspondence may be addressed. Email: pzhu@sjtu.edu.cn, daraio@caltech.edu, or weichen@northwestern.edu.

This article contains supporting information online at http://www.pnas.org/lookup/suppl/doi:10.1073/pnas.2122185119/-/DCSupplemental.

Published March 21, 2022.

Downloaded from https://www.pnas.org by California Institute of Technology on March 24, 2022 from IP address 131.215.101.152.

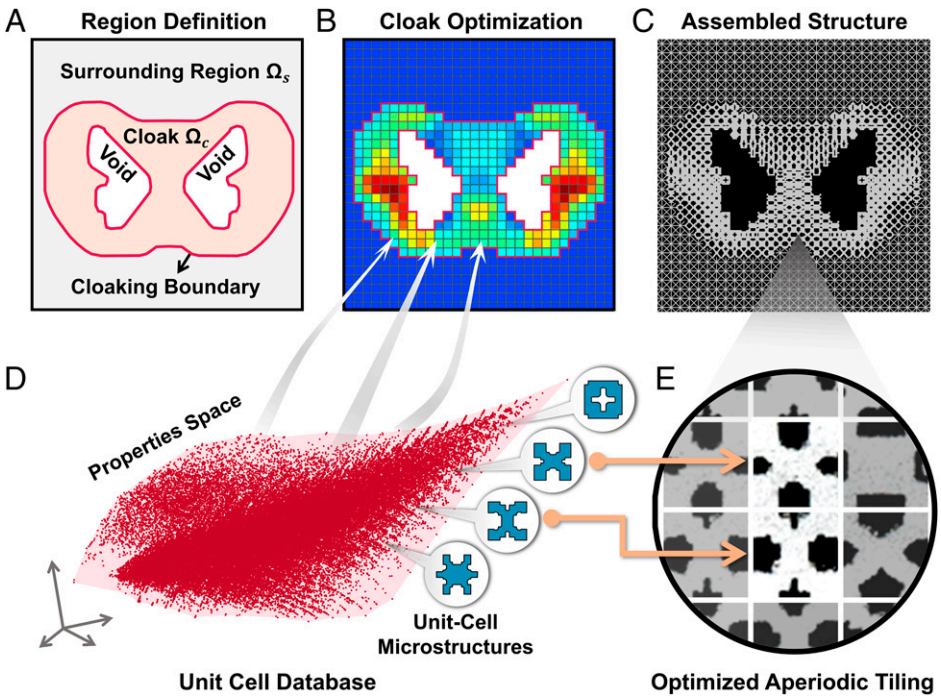

Fig. 1. Schematic diagram of the data-driven design of mechanical cloaks. (*A*) The region definition adopted in this study with voids, cloak, and surrounding region colored in white, orange, and gray, respectively. (*B*) Cloak optimization result, with both its topology (enclosed by red lines) and properties distribution (marked with gradient color) concurrently optimized. (*C*) The assembled structure (3D printed for validation) corresponding to the cloak optimization. (*D* and *E*) The properties space and representative unit-cell microstructures of the precomputed unit-cell database (*D*). It provides properties space to cloak optimization and candidate unit cells to achieve optimized aperiodic unit-cell tiling in the 3D-printed assembled structure (*E*).

Downloaded from https://www.pnas.org by California Institute of Technology on March 24, 2022 from IP address 131.215.101.152.

instead of effective material properties, within a prespecified cloak region (Fig. 1*A*) for simple shapes of voids. In another study, to simplify the mechanics featured by the high-rank elasticity tensor, special parameterized pentamode materials, with nearly zero shear modulus, were exploited in realizing an approximate elastomechanical core-shell cloak for a circular void (25). However, all of these methods are restricted to special types of parameterized lattices and can cloak only voids of simple shapes, i.e., circles and polygons. Moreover, the cloaking region must be prespecified and cannot accommodate voids or solid objects with arbitrary shapes. In this work, capitalizing on the recent advances in data-driven designs (29–31), we show that metamaterials with tessellated unit cells, selected from a precomputed database, can be used to obtain a more general cloaking design approach.

We focus on elastostatic cloaks that retain the same elastic displacement field in the homogeneous material initially around the void (labeled "surrounding region" in Fig. 1*A*). We propose a data-driven optimization method that capitalizes on a large and diverse precomputed metamaterial unit cell database. Our method concurrently optimizes the topology of the cloak and the distribution of metamaterial properties within the cloak. Based on this optimization, the method then assembles a physically fabricable structure made with different metamaterial unit cells through a tiling optimization process (31). By combining a large database with topology and properties optimization, this method can efficiently design cloaks to disguise multiple voids with complex shapes, in different homogeneous surroundings, under various boundary conditions, displaying superior flexibility compared to existing parametric design methods.

Results

As shown in Fig. 1*A*, we focus on the design of a mechanical cloak, Ω_c, around voids within the structure, that allows it to retain the displacement field in the surrounding region, Ω_s, as if there were no voids. As a result, the voids are "mechanically invisible" for observers located at any point within Ω_s, including both the boundaries and the insides. While our method can also accommodate cases that focus only on the boundaries, we choose to adopt this more general and challenging setting, as in most existing studies (24, 26–28), to demonstrate the flexibility of the proposed method. Practically, with this elastostatic cloak, voids could be intentionally introduced within a structure to realize special functions, e.g., to conceal underground tunnels, holes for wires, and cavities to hide objects, without affecting the structural integrity and functionality of the original structure. For instance, the cloak can be used in soft robots to keep the designed distorted postures unaffected by the voids and tunnels to place sensors or driving cables. To achieve this, as shown in Fig. 1*B*, we consider metamaterials within the structure as homogenized continua and then concurrently optimize the topology of the cloak, Ω_c, as well as the spatial distribution of the effective properties. Mathematically, we optimize the independent entries of the stiffness tensor, within the cloak Ω_c, to minimize the void-induced distortion of the displacement field in the surrounding region Ω_s (see *SI Appendix* for more details). For simplicity, we consider only unit cells with orthotropic symmetry in this study, whose stiffness tensor is calculated through energy-based homogenization and has four independent entries C_{11}, C_{12}, C_{22}, and C_{33} for two-dimensional (2D) design (in Voigt notation) (32, 33). To ensure the fabricability of the optimized materials, the properties are constrained within the properties space of a large and dense precomputed unit-cell database, during the optimization process (Fig. 1*D* and *SI Appendix*, Fig. S1). This precomputed database is generated by combining unit-cell topology optimization and a sequential stochastic shape perturbations algorithm to achieve shape and property diversities (see *SI Appendix* for

more details and access to the dataset) (34, 35). Unit cells with isolated pixels, checkerboard patterns, or features smaller than the predefined minimum length scale (0.5 mm) are filtered out to ensure the manufacturing feasibility. As demonstrated in *SI Appendix*, Fig. S2, the change of the mechanical properties in this precomputed database, i.e., stiffness tensor, is induced by the change of the unit-cell shapes only, without any modification to the constituent materials.

After the optimization, the cloak within the cloaking boundary is filled by an aperiodic tessellation of unit cells, selected to achieve the optimized properties distribution (Fig. 1*C* shows a printed assembled structure). Specifically, for each location in the cloak, we calculate the infinite norm of the difference between the optimized properties (C_{11}, C_{12}, C_{22}, and C_{33}) and properties of each unit cell in the precomputed database, which is denoted as θ_i. A set of unit cells is then selected from the database as candidates with the smallest θ_i values, whose properties are closest to the optimized local material properties. A tiling optimization is then performed to select the optimal unit cell from the candidate set in each location, to ensure good geometrical and mechanical compatibility between adjacent unit cells, as shown in Fig. 1*E*. In the tiling optimization, we use the ratio of the connected region versus the whole shared boundary to measure geometrical incompatibility. To reduce the possible deviation in the stiffness of a unit cell caused by the presence of a neighboring unit cell, we introduce the relative sum of stress difference on the shared boundary under the unit strain field to monitor the mechanical incompatibility. As a result, assembling a well-connected cloak with designed properties distribution can be achieved by selecting the best unit cell from the candidate set of each location to minimize the sum of properties difference θ_i, geometrical incompatibility measures, and mechanical incompatibility measures over the whole structure. This tiling optimization is formulated as an energy-minimization problem on a grid-like graph and solved efficiently by a dual decomposition method (see *SI Appendix* for more details) (36, 37). After the tiling optimization, the assembled structure with a cloak is obtained (Fig. 1*C*).

To demonstrate our approach, we first focus on the design of a cloak for a circular void, fixing the shape and size of the cloak. As shown in Fig. 2*A*, the reference structure (without voids and cloak) is composed of 30×30 periodically tessellated base cells, each of size 5×5 mm, whose constituent material has Young's modulus $E = 1.20$ GPa and Poisson's ratio $\nu = 0.35$. To facilitate displacement tracking in experimental measurement, a simple four-rod cubic lattice is chosen as the base cell (shown in Fig. 2 *A*, *Inset*). Its homogenized elastic properties, calculated through energy-based homogenization, are $C_{11} = 171.55$ MPa, $C_{12} = 69.68$ MPa, $C_{22} = 171.55$ MPa, and $C_{33} = 62.07$ MPa. Each unit cell is discretized into a 50×50 plane stress Q4 element. Finite-element simulations are then performed to calculate the displacement field of the reference structure under different boundary conditions (see *SI Appendix* for more details). We first model the response of the structure to a compressive load $u_{bc} = 0.5$ mm (0.67% average strain) in the horizontal direction, while keeping the top and bottom edges free (we refer to this configuration as a "displacement-free" boundary condition). The response of the material is assumed to remain linear elastic during the loading process. The resultant displacement fields in the homogeneous material, in both the x and y directions, are shown in Fig. 2 *B* and *C*, exhibiting a uniform transition from one end to the other. The presence of a circular void at the center of the structure (i.e., in the "voided structure"; Fig. 2*F*) causes a large distortion of the displacement field (Fig. 2 *G* and *H*), with significant shrinkage of the circular void. To control this distortion, we introduce a ring-shaped cloak, Ω_c, around the void, whose outer radius is twice the radius of the central void, as commonly used in the literature where the cloaking boundary is predefined (24). Later, we also present results when the cloaking boundary is not predefined but instead designed. The homogeneous medium outside the cloak in the structure, filled by periodic base cells as in the reference structure, is denoted as Ω_s. Using the proposed method, the cloak Ω_c is filled with aperiodic unit cells selected from the database to minimize the void-induced distortion of the displacement fields within the region Ω_s. We refer to this structure with a cloak surrounding the void as the "cloaked structure," which is shown in Fig. 2*K*. With our tiling optimization, neighboring unit cells retain good connections between each other, even though their properties and geometry vary. It is noted that the proposed optimization method allocates unit cells in a way that gradually increases the stiffness from the outer boundary to the inner one of the cloak Ω_c (Fig. 2 *K* and *P*). This gradient of stiffness compensates for the lack of structural cohesion due to the presence of the void, which is in line with existing mechanical cloak designs. Successful cloaking is evident when comparing the displacement fields of the reference structure, in Fig. 2 *B* and *C*, with the one in Ω_s of the cloaked structure, in Fig. 2 *L* and *M*. The large distortion of the central void is mitigated by the optimized cloak, displaying a gradual and uniform transition of displacement field along both x and y directions in the surrounding region Ω_s as that of the reference structure (i.e., without the void).

As a quantitative measure for the distortion of the displacement field, we opt for the commonly used relative displacement difference Δ formulated as

$$\Delta = \frac{\sqrt{\sum_{\Omega_s} \left(\vec{\boldsymbol{u}}_i - \vec{\boldsymbol{u}}_{0,i}\right)^2}}{\sqrt{\sum_{\Omega_s} \left(\vec{\boldsymbol{u}}_{0,i}\right)^2}}, \qquad [1]$$

where $\vec{\boldsymbol{u}}_i$ represents the nodal displacements of the finite elements in the cloaked (Fig. 2 *L* and *M*) or voided structure (Fig. 2 *G* and *H*), and $\vec{\boldsymbol{u}}_{0,i}$ represents the nodal displacements of the reference structure (Fig. 2 *B* and *C*). The summation operator performs the sum over all the nodes within the surrounding region Ω_s. The lower the relative displacement difference Δ, the smaller is the overall distortion of the displacement field from the reference state. With the designed cloak, the relative difference calculated from the numerical simulations is reduced from 17.20% in the voided structure to 4.00% in the cloaked structure, demonstrating a good cloaking performance.

To further validate the findings, we perform experiments on three-dimensional (3D)-printed structures, fabricated to reproduce 1) the reference structure, 2) the voided structure, and 3) the cloaked structure (Fig. 2*Q*). Considering the symmetry of the structure and the camera's field of view, we measure displacements from the upper left corner of each structure (Fig. 2*D*). Eq. 1 is used to calculate the relative displacement difference Δ in the experiment by inserting the measured displacements of the lattice points (centers of base cells) within the region Ω_s. Overall, the simulated and experimental displacements match well in terms of both displacement distribution (compare, e.g., Fig. 2 *A* and *B* with Fig. 2 *D* and *E* or Fig. 2 *G* and *H* with Fig. 2 *I* and *J*) and the relative displacement difference (reduced from 15.16% in the voided structure to 6.86% in the cloaked structure).

Downloaded from https://www.pnas.org by California Institute of Technology on March 24, 2022 from IP address 131.215.101.152.

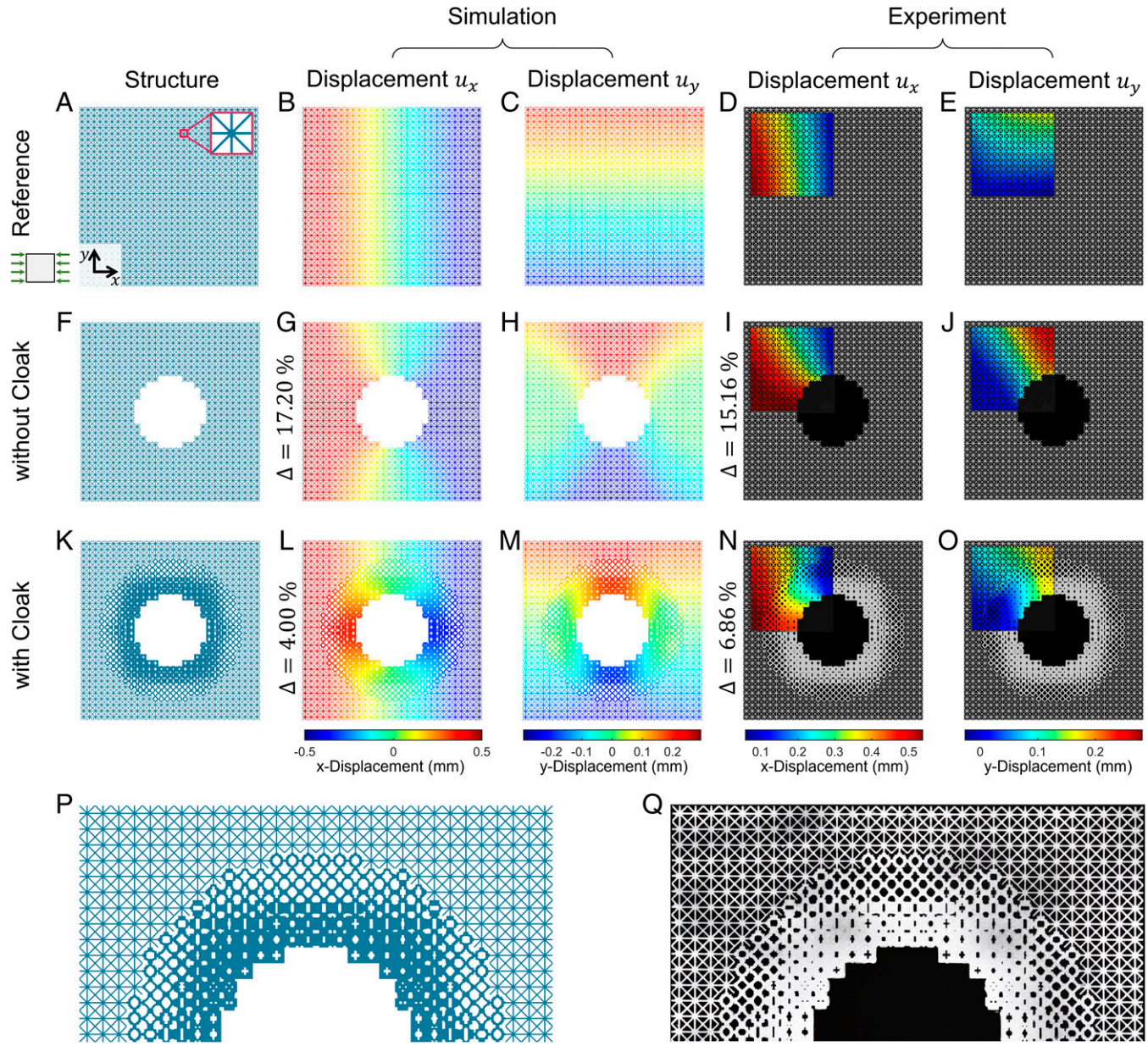

Fig. 2. Comparison of the numerical and experimental displacement fields obtained for the reference (*A–E*), voided (*F–J*), and cloaked (*K–O*) structures. *A*, *F*, and *K* show the geometry of the structures. *P* and *Q* show enlarged images of the upper half of the computationally designed and 3D physically printed cloaks, respectively. *A*, *Inset* shows the base cell of the reference structure. As shown in the schematic diagram in *A*, *Lower Left*, constant horizontal displacements are imposed on the left and right boundaries while keeping the other boundaries free.

The results shown in Fig. 2 are obtained under the displacement-free boundary condition. Nevertheless, our method is general and valid for various other boundary conditions. We demonstrate this by performing additional optimizations and numerical simulations with pressure-free, pressure-sliding, dilating, and shearing boundary conditions (Fig. 3 *A–F* and Movie S1). For the pressure-free boundary condition, we apply constant compressive pressure $p_{bc} = 95.67\,\mathrm{KPa}$ on the left and right edges, to keep the average strain around 1% and ensure that the structure remains in the linear elastic deformation range. The proposed optimization method generates a cloaked structure shown in Fig. 3*C*, with a similar stiffness gradient as observed in the design obtained for the previous displacement-free boundary condition (Fig. 2 *K*, *P*, and *Q*). As shown in the first two bar groups in Fig. 3*B*, the relative displacement difference of the voided structure is much higher for the pressure-free boundary condition (102.3%) than that of the previous displacement-free boundary condition (17.2%). This is because, in contrast to the displacement-free boundary condition, the pressure-free boundary condition allows nonuniform displacements on the left and right boundaries, which encourages the shrinkage of the void after the loading (*SI Appendix*, Fig. S6). Nevertheless, the cloaked structure obtained can still effectively reduce the distortion caused by the void to a $\Delta = 12.8\%$. Adding an extra sliding boundary condition on the top and bottom in the pressure-free boundary condition leads to the pressure-sliding boundary condition. Under this condition, the constraints imposed by the sliding support compress the structure against Poisson's-effect–induced expansion in the vertical direction. As a result, compared with the previous single-directional loading cases (displacement-free and pressure-free), the joint effects of the support reactions and imposed pressure enable the

Downloaded from https://www.pnas.org by California Institute of Technology on March 24, 2022 from IP address 131.215.101.152.

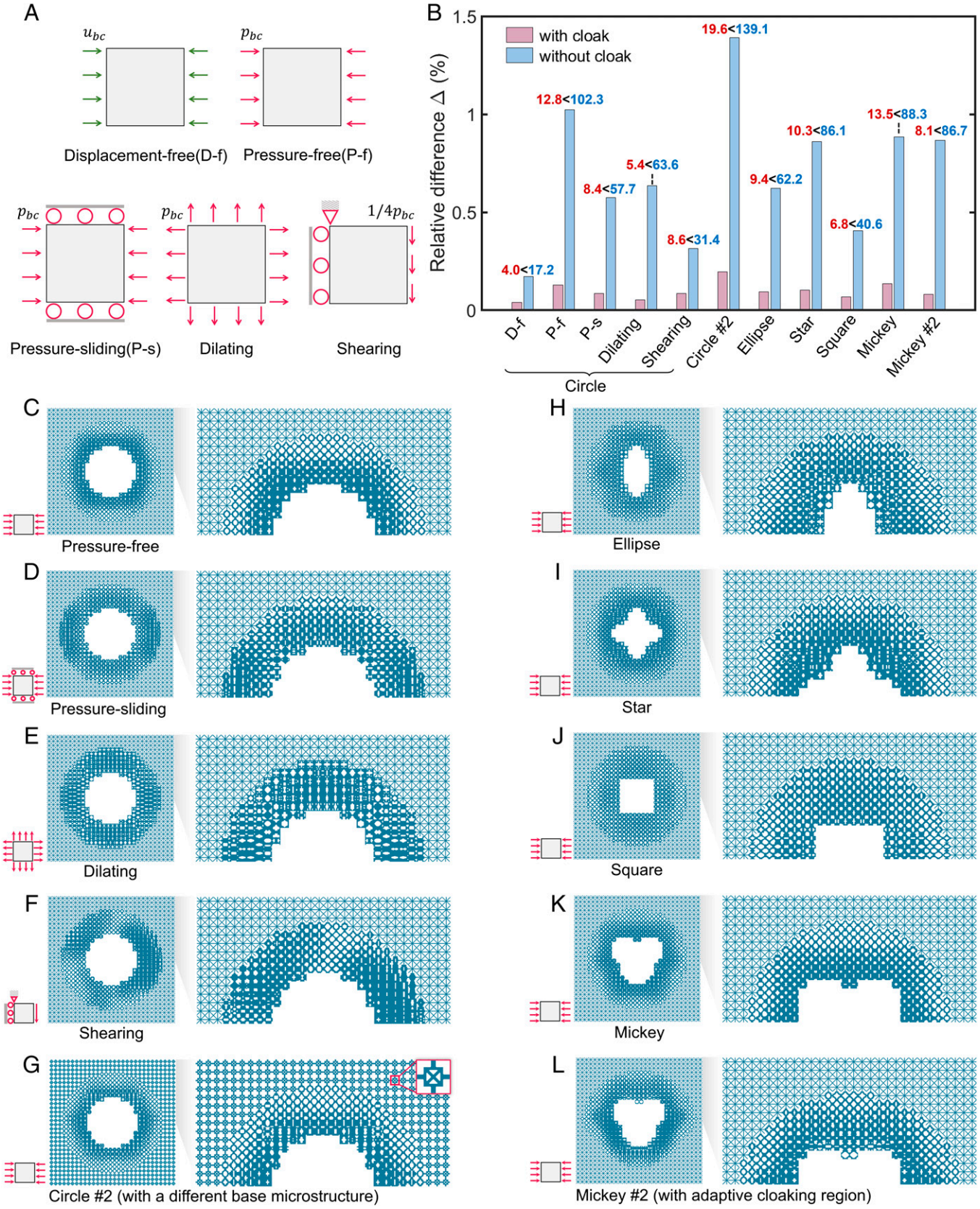

Fig. 3. Design results for different boundary conditions and shapes of the void and a different type of base cell. (*A*) Different boundary conditions analyzed. (*B*) Bar graph for the relative displacement differences of different voided (values colored in red) and cloaked structures (values colored in blue). (*C*–*F*) Cloaked structures for a circular void under (*C*) pressure-free boundary condition, (*D*) pressure-sliding boundary condition, (*E*) dilating boundary condition, and (*F*) shearing boundary condition. (*G*) Cloaked structure for a circular void under pressure-free boundary condition with the second type of base cell shown in *Inset* of the enlarged image (*Right*). (*H*–*K*) cloaked structures for different shapes of voids under the same pressure-free boundary condition. (*L*) Cloaked structure for a Mickey-shaped void under the pressure-free boundary condition with the optimized topology of the cloak. Enlarged images of the upper half of cloaked structures are shown in *C*–*L*, *Right*.

Downloaded from https://www.pnas.org by California Institute of Technology on March 24, 2022 from IP address 131.215.101.152.

void-induced distortion to cover a larger area in the structure (*SI Appendix*, Fig. S7). Therefore, the optimized cloak contains more unit cells with high stiffness (Fig. 3*D* and *SI Appendix*, Fig. S7), to balance the strains and suppress the shrinkage of the void. The expansion of the high stiffness region is even more obvious under the dilating boundary condition (Fig. 3*E*). This is because, under this boundary condition, the affected area of the distortion in the voided structure is even larger with the uniformly distributed stretching force exerted from all four edges (*SI Appendix*, Fig. S8). Similarly, for the shearing boundary condition, large void-induced distortions of the displacement field mainly distribute in the right half of the structure (*SI Appendix*, Fig. S9), corresponding to regions with stiffer unit cells in the cloak (Fig. 3*F*). Nevertheless, neighboring unit cells in the cloak remain well connected for these three boundary conditions with our tiling optimization, achieving excellent cloaking performance with low relative errors (<9%), as shown in the third through fifth bar groups in Fig. 3*B*. Note that all the cloak designs shown in this study remain effective for other magnitudes of compressive pressure or displacement imposed on the boundary, as long as the deformation remains in the regime of linear elasticity. This is because, in linear elasticity, the relative displacement difference, Δ, does not depend on the absolute magnitude of the loading.

While most existing design methods for mechanical cloaks confine the base cell in the surrounding region to bimode or simple parameterized lattice, the proposed method can systematically accommodate various free-formed base cells. As an example, we use a different type of unit cell with more complex geometry as the base cell and consider a circular void under the pressure-free boundary condition (Fig. 3*G*). The homogenized stiffness tensor of this base cell yields $C_{11} = 123.02$ MPa, $C_{12} = 48.02$ MPa, $C_{22} = 123.02$ MPa, and $C_{33} = 13.50$ MPa. As shown by the simulated displacement field (*SI Appendix*, Fig. S10 and Movie S2) and the large relative displacement difference of the voided structure (Fig. 3*B*), this type of compliant base cell leads to a significant amount of distortion of the displacement field. Yet, the proposed method can still effectively reduce the relative error from 139.1% to 19.6% with the optimized cloak. Moreover, it should be noted that the proposed method can also design the same cloak to accommodate various loading cases by aggregating individual cloaking performance into an overall objective function. For example, we obtain a cloak that achieves excellent cloaking performance ($\Delta < 15\%$) for constant distributed loading imposed from any angle (*SI Appendix*, Figs. S11 and S12), by using a p-norm–based aggregated objective function in the optimization (see *SI Appendix* for more details).

Unlike design methods based on the material-parameter transform or direct lattice transform, the proposed method can also be applied to create cloaks around voids with arbitrary shapes (Fig. 3 *H–K*; *SI Appendix*, Fig. S13; and Movie S3), due to either functional or aesthetic needs. We demonstrate this capability by designing cloaks for different voids, applying the same pressure-free boundary condition and predefined cloak topology, as in Fig. 2. Similar to our previous designs for a circular void, the stiffness of the unit cells within these optimized cloaks (Fig. 3 *H–K*) exhibits a decreasing trend starting from the edge of the void to the outer boundary of the cloak. From Fig. 3*B* and *SI Appendix*, Fig. S13, it can be noted that the various optimized cloaks reduce distortion of the displacement fields induced by the voids of various shapes, keeping relative displacement difference at a considerably low level (~6.8% to 13.5%). It is interesting to note that the cloaked structures for inclusions with high aspect ratios and sharp corners (Fig. 3 *H–J*) can achieve better cloaking performance than that of circular and Mickey-shaped inclusions (Fig. 3 *C* and *K*). This might be due to a smaller ratio of inclusion to the cloaking region for structures in Fig. 3 *H–J* than that for structures in Fig. 3 *C* and *K*. It also demonstrates the applicability of the proposed method for inclusions with less regular shapes. It should be pointed out that, while the circular void in Fig. 3*C* could geometrically enclose voids of various shapes in Fig. 3 *H–J*, the solution is less optimal or efficient compared to the cloaking design optimized specifically for a desired shape of voids.

In all results discussed so far, a predefined cloaking boundary of the cloak is used and remains unchanged during the design process. This is a requirement similar to most existing methods (24–26, 28). We present next that our proposed method can also simultaneously design the topology, i.e., free-formed geometry that allows topological changes, of the cloaking region Ω_c and the property distribution within it, adapting to different geometries of voids. To demonstrate the benefits of not predefining the cloaking boundary, based on the Mickey-shaped void, we limit the area of the cloak to be equal to that of the previously used circular one, while concurrently optimizing the topology and its property distribution to minimize the relative displacement difference (Movie S4). The resulting cloaked structure and its displacement field are shown in Fig. 3*L* and *SI Appendix*, Fig. S13, respectively. We observe that the cloaking boundary conforms to the contour of the Mickey-shaped void, expanding in the upper half and shrinking in the lower half. As shown in Fig. 3*B*, while the relative displacement differences are similar for the voided structures with the predefined (88.3%) and optimized topologies of cloaks (86.7%), the cloak with optimized topology can achieve a much smaller relative error (8.1%) than the cloak with predefined topology (13.5%).

To further demonstrate the versatility of the proposed method, we design a cloak for two voids arranged in a butterfly shape, subjected to the displacement-free boundary condition, as shown in Fig. 4. The specialty of this example lies in that there are two neighboring irregular voids (Fig. 4*F*), which cannot be decomposed into simple ellipses or squares. The existence of multiple voids and the mechanical interaction between them poses an additional challenge to the adaptive design of mechanical cloaks. As shown in Fig. 4 *G–J* and Movie S5, both the simulated and experimental results suggest that the butterfly-shaped voids distort the displacement field significantly, especially along the y direction. The cloaked structure designed by the proposed method successfully reduced the relative difference Δ nearly by half for both calculated and experimental results, leading to a displacement field (Fig. 4 *L–O*) close enough to that of the reference structure (Fig. 4 *B–E*).

Conclusion

In this study, we have developed a data-driven method for the design of mechanical cloaks, powered by topology optimization. This method first optimizes the shape and topology of the cloak and the material property distributions within the cloak and then selects optimal unit cells from a precomputed database of material microstructures to fill the cloak through an efficient optimization-based tiling process. Using multiple examples with various numbers and shapes of voids, boundary conditions, and base cells, we demonstrate that our method achieves excellent performance in mechanical cloaking, verified both numerically and experimentally. Compared to existing approaches that are applicable only to a fixed but restricted topology of cloaks, our method is capable of concurrently

Downloaded from https://www.pnas.org by California Institute of Technology on March 24, 2022 from IP address 131.215.101.152.

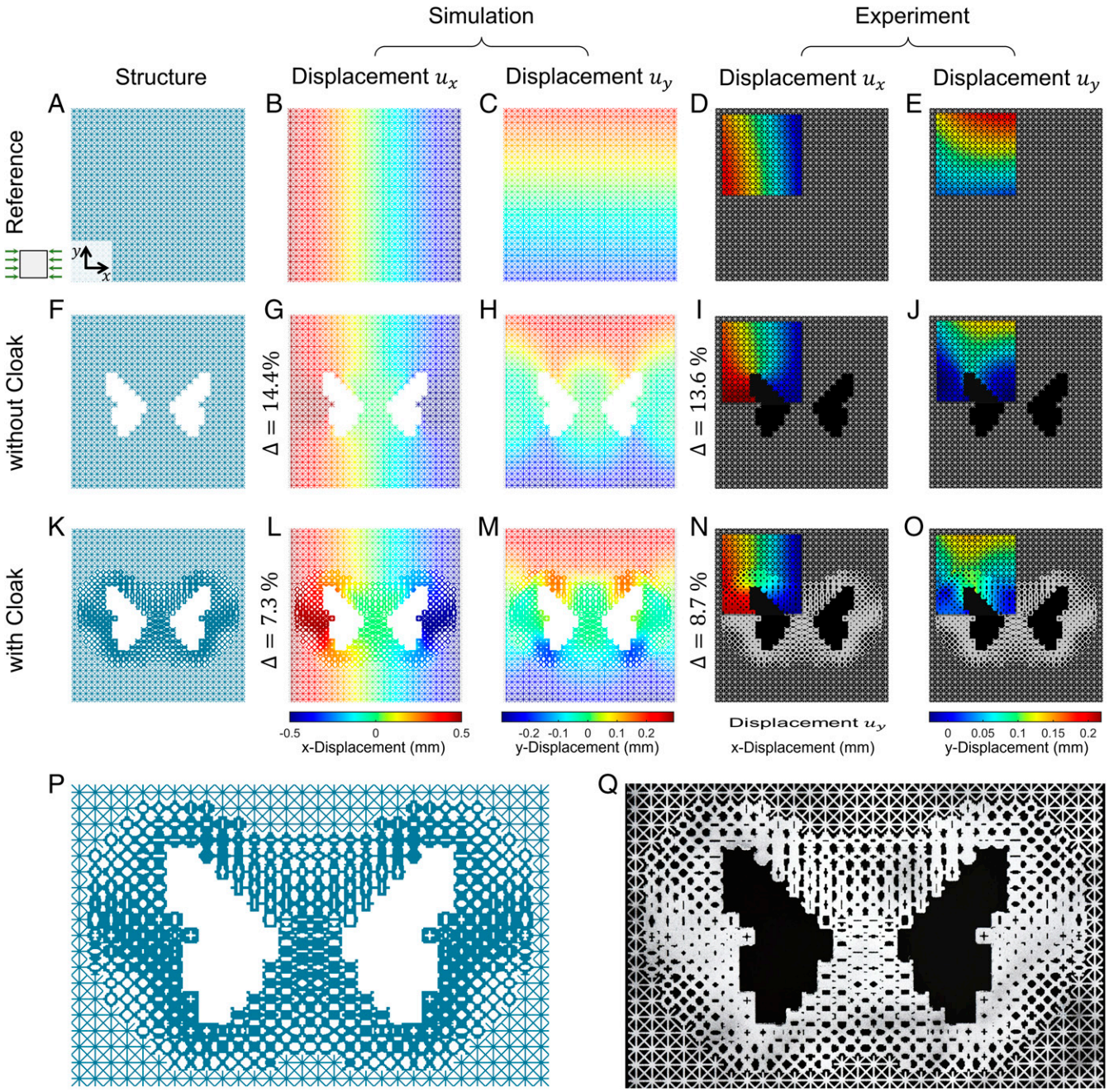

Fig. 4. (*A*–*O*) Geometries, calculated and experimentally measured displacement fields for reference, and voided and cloaked structures as in Fig. 2, but with butterfly-shaped voids and optimized topology of the cloak. *P* and *Q* show enlarged images of the designed and 3D-printed cloaks, respectively.

designing the topology and property distribution of the cloak, balancing both efficiency and versatility. We observe that the optimized topology of the cloak generally conforms to the contour of different geometries of voids, providing a better cloaking performance compared to cloak designs with fixed topology. While we focus only on voids in this study, the proposed method can be readily applied to the cloak design for solid inclusions with stiffness lower than that of the base cell, which induces smaller loss of structural integrity and thus more easily achieves good cloaking performance. Our method can also handle solid inclusions with a higher stiffness than that of the base cell but will require more compliant unit cells to be included in the database. The data-driven approach is powerful in terms of its capability to swiftly respond to new design scenarios with limited computational cost, by taking advantage of the rich unit-cell database that is readily available. In the preparation of the databases, we can also easily take into account manufacturability and other resource restrictions.

Methods

The design of each unit cell in the database is pixelated and represented by a 50×50 binary matrix. We follow the common practice in multiscale topology optimization to use a corresponding 50×50 four-node quadrilateral plane stress finite-element mesh for each unit cell in the full structure. Because the maximal strain of the assembled structure is ∼1% to 2%, the finite-element analysis is carried out in MATLAB and ABAQUS under the linear elasticity and plane stress assumptions. The good agreement between the numerical calculation and the experimental measurement validates the effectiveness of the calculation method.

Downloaded from https://www.pnas.org by California Institute of Technology on March 24, 2022 from IP address 131.215.101.152.

We fabricated all the structures tested using a Stratasys Connex Objet 500 3D printer. We subjected the structures to compression using an Instron E3000 machine. While the structures were being loaded, we captured a sequence of images using a Nikon D750 camera mounted with a Nikkor 200-mm f/4D IF-ED lens. Digital image correlation (DIC) on the captured images was performed with a global DIC code designed specifically for two-dimensional materials with microstructures (38).

More details on the design methods and experiments can be found in *SI Appendix*.

Data Availability. Data (2D orthotropic metamaterial microstructrue dataset) have been deposited in Figshare (https://doi.org/10.6084/m9.figshare.17141975.v1).

ACKNOWLEDGMENTS. We are grateful for support from the NSF Cyberinfrastructure for Sustained Scientific Innovation program (Grant OAC 1835782) and Center for Hierarchical Materials Design (National Institute of Standards and Technology [NIST] 70NANB19H005). L.W. acknowledges support from the Zhiyuan Honors Program for Graduate Students of Shanghai Jiao Tong University for his predoctoral visiting study at Northwestern University.

1. M. Wegener, Materials science. Metamaterials beyond optics. *Science* **342**, 939–940 (2013).
2. N. I. Zheludev, Applied physics. The road ahead for metamaterials. *Science* **328**, 582–583 (2010).
3. X. Yu, J. Zhou, H. Liang, Z. Jiang, L. Wu, Mechanical metamaterials associated with stiffness, rigidity and compressibility: A brief review. *Prog. Mater. Sci.* **94**, 114–173 (2018).
4. M. Kadic, G. W. Milton, M. van Hecke, M. Wegener, 3D metamaterials. *Nat. Rev. Phys.* **1**, 198–210 (2019).
5. D. R. Reid *et al.*, Auxetic metamaterials from disordered networks. *Proc. Natl. Acad. Sci. U.S.A.* **115**, E1384–E1390 (2018).
6. T. S. Lumpe, T. Stankovic, Exploring the property space of periodic cellular structures based on crystal networks. *Proc. Natl. Acad. Sci. U.S.A.* **118**, e2003504118 (2021).
7. U. Leonhardt, Optical conformal mapping. *Science* **312**, 1777–1780 (2006).
8. A. Greenleaf, Y. Kurylev, M. Lassas, U. Leonhardt, G. Uhlmann, Cloaked electromagnetic, acoustic, and quantum amplifiers via transformation optics. *Proc. Natl. Acad. Sci. U.S.A.* **109**, 10169–10174 (2012).
9. B. Jenett *et al.*, Discretely assembled mechanical metamaterials. *Sci. Adv.* **6**, eabc9943 (2020).
10. A. Rafsanjani, Y. Zhang, B. Liu, S. M. Rubinstein, K. Bertoldi, Kirigami skins make a simple soft actuator crawl. *Sci. Robot.* **3**, eaar7555 (2018).
11. A. Lamoureux, K. Lee, M. Shlian, S. R. Forrest, M. Shtein, Dynamic kirigami structures for integrated solar tracking. *Nat. Commun.* **6**, 8092 (2015).
12. N. Kaina, F. Lemoult, M. Fink, G. Lerosey, Negative refractive index and acoustic superlens from multiple scattering in single negative metamaterials. *Nature* **525**, 77–81 (2015).
13. Y. Yang *et al.*, Full-polarization 3D metasurface cloak with preserved amplitude and phase. *Adv. Mater.* **28**, 6866–6871 (2016).
14. S. Narayana, Y. Sato, DC magnetic cloak. *Adv. Mater.* **24**, 71–74 (2012).
15. J. B. Pendry, D. Schurig, D. R. Smith, Controlling electromagnetic fields. *Science* **312**, 1780–1782 (2006).
16. L. Xu, H. Chen, Conformal transformation optics. *Nat. Photonics* **9**, 15–23 (2015).
17. H. Chen, C. T. Chan, P. Sheng, Transformation optics and metamaterials. *Nat. Mater.* **9**, 387–396 (2010).
18. U. Leonhardt, Notes on conformal invisibility devices. *New J. Phys.* **8**, 118 (2006).
19. W. Cai, U. K. Chettiar, A. V. Kildishev, V. M. Shalaev, Optical cloaking with metamaterials. *Nat. Photonics* **1**, 224–227 (2007).
20. F. Yang, Z. L. Mei, T. Y. Jin, T. J. Cui, DC electric invisibility cloak. *Phys. Rev. Lett.* **109**, 053902 (2012).
21. R. Schittny, M. Kadic, S. Guenneau, M. Wegener, Experiments on transformation thermodynamics: Molding the flow of heat. *Phys. Rev. Lett.* **110**, 195901 (2013).
22. T. Chen, C.-N. Weng, Y.-L. Tsai, Materials with constant anisotropic conductivity as a thermal cloak or concentrator. *J. Appl. Phys.* **117**, 054904 (2015).
23. G. W. Milton, M. Briane, J. R. Willis, On cloaking for elasticity and physical equations with a transformation invariant form. *New J. Phys.* **8**, 248 (2006).
24. T. Bückmann, M. Kadic, R. Schittny, M. Wegener, Mechanical cloak design by direct lattice transformation. *Proc. Natl. Acad. Sci. U.S.A.* **112**, 4930–4934 (2015).
25. T. Bückmann, M. Thiel, M. Kadic, R. Schittny, M. Wegener, An elasto-mechanical unfeelability cloak made of pentamode metamaterials. *Nat. Commun.* **5**, 4130 (2014).
26. L. Hai, Q. Zhao, Y. Meng, Unfeelable mechanical cloak based on proportional parameter transform in bimode structures. *Adv. Funct. Mater.* **28**, 1801473 (2018).
27. X. Xu *et al.*, Physical realization of elastic cloaking with a polar material. *Phys. Rev. Lett.* **124**, 114301 (2020).
28. M. Kadic *et al.*, Elastodynamic behavior of mechanical cloaks designed by direct lattice transformations. *Wave Motion* **92**, 102419 (2020).
29. C. Schumacher *et al.*, Microstructures to control elasticity in 3D printing. *ACM Trans. Graph.* **34**, 1–13 (2015).
30. B. Zhu, M. Skouras, D. Chen, W. Matusik, Two-scale topology optimization with microstructures. *ACM Trans. Graph.* **36**, 1 (2017).
31. L. Wang *et al.*, Deep generative modeling for mechanistic-based learning and design of metamaterial systems. *Comput. Methods Appl. Mech. Eng.* **372**, 113377 (2020).
32. Z. Hashin, Analysis of composite materials–A survey. *J. Appl. Mech.* **50**, 481 (1983).
33. L. Xia, P. Breitkopf, Design of materials using topology optimization and energy-based homogenization approach in Matlab. *Struct. Multidiscipl. Optim.* **52**, 1229–1241 (2015).
34. L. Wang *et al.*, 2D orthotropic metamaterial micorstructrue dataset. Figshare. https://doi.org/10.6084/m9.figshare.17141975.v1. Deposited 12 August 2021.
35. L. Wang, Y.-C. Chan, Z. Liu, P. Zhu, W. Chen, Data-driven metamaterial design with Laplace-Beltrami spectrum as "shape-DNA". *Struct. Multidiscipl. Optim.* **61**, 2613–2628 (2020).
36. C. Wang, N. Komodakis, N. Paragios, Markov random field modeling, inference & learning in computer vision & image understanding: A survey. *Comput. Vis. Image Underst.* **117**, 1610–1627 (2013).
37. N. Komodakis, N. Paragios, G. Tziritas, MRF energy minimization and beyond via dual decomposition. *IEEE Trans. Pattern Anal. Mach. Intell.* **33**, 531–552 (2011).
38. F. Agnelli, P. Margerit, P. Celli, C. Daraio, A. Constantinescu, Systematic two-scale image analysis of extreme deformations in soft architectured sheets. *Int. J. Mech. Sci.* **194**, 106205 (2021).

Downloaded from https://www.pnas.org by California Institute of Technology on March 24, 2022 from IP address 131.215.101.152.